SARS-coronavirus-2 replication in Vero E6 cells: replication kinetics, rapid adaptation and cytopathology

Natacha S. Ogando[1], Tim J. Dalebout[1], Jessika C. Zevenhoven-Dobbe[1], Ronald W. Limpens[2], Yvonne van der Meer[1], Leon Caly[3], Julian Druce[3], Jutte J. C. de Vries[4], Marjolein Kikkert[1], Montserrat Bárcena[2], Igor Sidorov[1] and Eric J. Snijder[1]

[1] Molecular Virology Laboratory, Department of Medical Microbiology, Leiden University Medical Center, Leiden, the Netherlands
[2] Section Electron Microscopy, Department of Cell and Chemical Biology, Leiden University Medical Center, Leiden, the Netherlands
[3] Virus Identification Laboratory, Victorian Infectious Diseases Reference Laboratory, Doherty Institute, Melbourne, Australia
[4] Clinical Microbiology Laboratory, Department of Medical Microbiology, Leiden University Medical Center, Leiden, the Netherlands

This paper is dedicated to the loving memory of

José Manuel Ogando Fernandes Pereira (72) and María de los Ángeles Martín (93)

who succumbed to SARS-CoV-2 infection on March 27 and 28, 2020.

Corresponding author: Eric J. Snijder (e.j.snijder@lumc.nl)

Keywords: plaque phenotype, evolution, RNA synthesis, antisera, furin cleavage site, antiviral drugs

Abbreviations: SARS-CoV, severe acute respiratory syndrome coronavirus; CoV, Coronavirus; CPE, cytopathic effect; HCoV, human coronavirus; MERS-CoV, Middle East respiratory syndrome coronavirus;; nsp, non-structural protein; S protein, spike protein; ACE2, angiotensin-converting enzyme 2; NGS, next-generation sequencing; RO, replication organelle; DMV, Double-membrane vesicle; PEG-IFN-α, pegylated interferon alpha; UTR, untranslated region.

ABSTRACT

The sudden emergence of severe acute respiratory syndrome coronavirus 2 (SARS-CoV-2) at the end of 2019 from the Chinese province of Hubei and its subsequent pandemic spread highlight the importance of understanding the full molecular details of coronavirus infection and pathogenesis. Here, we compared a variety of replication features of SARS-CoV-2 and SARS-CoV and analysed the cytopathology caused by the two closely related viruses in the commonly used Vero E6 cell line. Compared to SARS-CoV, SARS-CoV-2 generated higher levels of intracellular viral RNA, but strikingly about 50-fold less infectious viral progeny was recovered from the culture medium. Immunofluorescence microscopy of SARS-CoV-2-infected cells established extensive cross-reactivity of antisera previously raised against a variety of nonstructural proteins, membrane and nucleocapsid protein of SARS-CoV. Electron microscopy revealed that the ultrastructural changes induced by the two SARS viruses are very similar and occur within comparable time frames after infection. Furthermore, we determined that the sensitivity of the two viruses to three established inhibitors of coronavirus replication (Remdesivir, Alisporivir and chloroquine) is very similar, but that SARS-CoV-2 infection was substantially more sensitive to pre-treatment of cells with pegylated interferon alpha. An important difference between the two viruses is the fact that - upon passaging in Vero E6 cells - SARS-CoV-2 apparently is under strong selection pressure to acquire adaptive mutations in its spike protein gene. These mutations change or delete a putative ‘furin-like cleavage site’ in the region connecting the S1 and S2 domains and result in a very prominent phenotypic change in plaque assays.

INTRODUCTION

For the first time in a century, societies and economies worldwide have come to a near-complete standstill due to a pandemic outbreak of a single RNA virus. This virus, the severe acute respiratory syndrome coronavirus 2 (SARS-CoV-2) (1) belongs to the coronavirus (CoV) family, which is thought to have given rise to zoonotic introductions on multiple previous occasions during the past centuries. Coronaviruses are abundantly present in mammalian reservoir species, including bats (2), and should now be recognized definitively as a continuous zoonotic threat with the ability to cause severe human disease and explosive pandemic transmission.

To date, seven CoVs that can infect humans have been identified, which segregate into two classes. On the one hand, there are four endemic human CoVs (HCoVs), the first of which were identified in the 1960's, annually causing a substantial number of common colds (3, 4). On the other hand, we now know of (at least) three zoonotic CoVs that have caused outbreaks in the human population recently: severe acute respiratory syndrome coronavirus (SARS-CoV) (5, 6) in 2002-2003, Middle East respiratory syndrome-coronavirus (MERS-CoV) (7, 8) since 2012 (and probably earlier) and the currently pandemic SARS-CoV-2 (9, 10). The latter agent emerged near Wuhan (People's Republic of China) in the fall of 2019 and its animal source is currently under investigation (11-13). Transmission to humans of SARS-CoV and MERS-CoV was attributed to civet cats (14) and dromedary camels (15), respectively, although both species may have served merely as an intermediate host due to their close contact with humans. All three zoonotic CoVs belong to the genus *betacoronavirus* (beta-CoV), which is abundantly represented among the CoVs that circulate in the many bat species on this planet (2, 16-19). The genetic diversity of bat CoVs and their phylogenetic relationships with the four known endemic HCoVs (OC43, HKU1, 229E and NL63; the latter two being alpha-CoVs) suggests that also these may have their evolutionary origins in bat hosts, for most of them probably centuries ago (20).The potential of multiple CoVs from different genera to cross-species barriers had been predicted and documented previously (2, 16-19, 21, 22),

but regrettably was not taken seriously enough to invest more extensively in prophylactic and therapeutic solutions that could have contributed to rapidly containing an outbreak of the current magnitude.

Compared to other RNA viruses, CoVs possess an unusually large positive-sense RNA genome with a size ranging from 26 to 34 kilobases (23). The CoV genome is single-stranded and its 5'-proximal two-thirds encode for the large and partially overlapping replicase polyproteins pp1a and pp1ab (4,000-4,500 and 6,700-7,200 amino acids long, respectively), with the latter being a C-terminally extended version of the former that results from ribosomal frameshifting. The replicase polyproteins are processed into 16 cleavage products (non-structural proteins, nsps) by two internal proteases, the papain-like protease (PL^{pro}) in nsp3 and the 3C-like or 'main' protease (M^{pro}) in nsp5 (24). Specific trans-membrane nsps (nsp3, 4 and 6) than cooperate to transform intracellular membranes into a viral replication organelle (RO) (25) that serves to organize and execute CoV RNA synthesis, which entails genome replication and the synthesis of an extensive nested set of subgenomic (sg) mRNAs. The latter are used to express the genes present in the 3'-proximal third of the genome, which encode the four common CoV structural proteins (spike (S), envelope (E), membrane (M) and nucleocapsid (N) protein) and the 'so-called' accessory protein genes, most of which are thought to be involved in the modulation of host responses to CoV infection (26). The CoV proteome includes a variety of potential targets for drug repurposing or *de novo* development of specific inhibitors of e.g. viral entry (S protein) or RNA synthesis (27). The latter process depends on a set of enzymatic activities (24) including an RNA-dependent RNA polymerase (RdRp; in nsp12), RNA helicase (in nsp13), two methyltransferases involved in mRNA capping (a guanine-N7-methyltranferase in nsp14 and a nucleoside-2'-O-methyltransferase in nsp16) and a unique exoribonuclease (ExoN, in nsp14) that promotes the fidelity of the replication of the large CoV genome (28). Other potential drug targets are the transmembrane proteins that direct the formation of the viral RO, several less well characterised enzymatic activities and a

112 set of smaller nsps (nsp7-10) that mainly appear to serve as cofactors/modulators of other
113 nsps.

114 The newly emerged SARS-CoV-2 was rapidly identified as a CoV that is relatively closely
115 related to the 2003 SARS-CoV (9, 29, 30).The two genome sequences are about ~80%
116 identical and the organization of open reading frames is essentially the same. The overall level
117 of amino acid sequence identity of viral proteins ranges from about 65% in the least conserved
118 parts of the S protein to about 95% in the most conserved replicative enzyme domains,
119 prompting the coronavirus study group of the International Committee on the Taxonomy of
120 Viruses to classify the new agent within the species *Severe acute respiratory syndrome-*
121 *related coronavirus*, which also includes the 2003 SARS-CoV (1). The close phylogenetic
122 relationship also implies that much of our knowledge of SARS-CoV molecular biology,
123 accumulated over the past 17 years, can probably be translated to SARS-CoV-2. Many reports
124 posted over the past months have described such similarities, including the common affinity
125 of the two viruses for the angiotensin-converting enzyme 2 (ACE2) receptor (9, 31). This
126 receptor is abundantly expressed in Vero cells (African green monkey kidney cells). Since
127 2003, Vero cells have been used extensively for SARS-CoV research in cell culture-based
128 infection models by many laboratories, including our own.

129 We set out to establish the basic features of SARS-CoV-2 replication in Vero cells and
130 compare it to the Frankfurt-1 SARS-CoV isolate from 2003 (32, 33) . When requesting virus
131 isolates (February 2020), and in spite of the rapidly emerging public health crisis, we were
132 confronted - not for the first time - with administrative hurdles and discussions regarding the
133 alleged ‘ownership’ of virus isolates cultured from (anonymous) clinical samples. From a
134 biological and evolutionary point of view, this would seem a strangely anthropocentric
135 consideration, but it ultimately forced us to reach out across the globe to Australian colleagues
136 in Melbourne. After checking our credentials and completing a basic material transfer
137 agreement, they provided us (within one week) with their first SARS-CoV-2 isolate (originally
138 named 2019-nCoV/Victoria/1/2020 and subsequently renamed

BetaCoV/Australia/VIC01/2020; (34), which will be used throughout this study. Until now, this isolate has been provided to 17 other laboratories worldwide to promote the rapid characterization of SARS-CoV-2, in this critical time of lockdowns and other preventive measures to avoid a collapse of public health systems.

In this report, we describe a comparative study of the basic replication features of SARS-CoV and SARS-CoV-2 in Vero E6 cells, including growth kinetics, virus titres, plaque phenotype and an analysis of intracellular viral RNA and protein synthesis. Additionally, we analysed infected cells by light and electron microscopy, and demonstrated cross-reactivity of 13 available SARS-CoV-specific antisera (recognising 10 different viral proteins) with their SARS-CoV-2 counterparts. Finally, we established the conditions for a medium-throughput assay to evaluate basic antiviral activity and assessed the impact of some known CoV inhibitors on SARS-CoV-2 replication. In addition to many anticipated similarities, our results also established some remarkable differences between the two viruses that warrant further investigation. One of them is the rapid evolution - during virus passaging in Vero cells - of a specific region of the SARS-CoV-2 S protein that contains the so-called 'furin-like cleavage site'.

METHODS

Cell and virus culture

Vero E6 cells and HuH7 cells were grown as described previously (35). SARS-CoV-2 isolate Australia/VIC01/2020 (GeneBank ID: MT007544.1; (34)) was derived from a positively-testing nasopharyngeal swab in Melbourne, Australia, and was propagated twice in Vero/hSLAM cells, before being shared with other laboratories. In Leiden, the virus was passaged two more times at low multiplicity of infection (m.o.i.) in Vero E6 cells to obtain a working stock (p2 stock). SARS-CoV isolate Frankfurt 1 (36) was used to compare growth kinetics and other features

with SARS-CoV-2. Infection of Vero E6 cells was carried out in phosphate-buffered saline (PBS) containing 50 µg/ml DEAE-dextran and 2% fetal calf serum (FCS; Bodinco). The inoculum was added to the cells for 1 h at 37°C, after which cells were washed twice with PBS and maintained in Eagle's minimal essential medium (EMEM; Lonza) with 2% FCS, 2mM L-glutamine (PAA) and antibiotics (Sigma). Viral titres were determined by plaque assay in Vero E6 cells as described previously (37). For plaque picking, plaque assays were performed using our p1 stock, while using an overlay containing 1% of agarose instead of Avicel (RC-581; FMC Biopolymer). Following neutral red staining, small and large plaques were picked and used to inoculate a 9.6-cm^2 dish of Vero E6 cells containing 2 ml of EMEM-2%FCS medium, yielding p1 virus. After 48 h, 200 µl of the culture supernatant was used to infect the next dish of cells (p2), a step that was repeated one more time to obtain p3 virus. All work with live SARS-CoV and SARS-CoV-2 was performed in biosafety laboratory level 3 facilities at Leiden University Medical Center, the Netherlands.

Analysis of intracellular viral RNA and protein synthesis

Isolation of intracellular RNA was performed by lysing infected cell monolayers with TriPure isolation reagent (Roche Applied Science) according to the manufacturer's instructions. After purification and ethanol precipitation, intracellular RNA samples were loaded onto a 1.5% agarose gel containing 2.2 M formaldehyde, which was run overnight at low voltage overnight in MOPS buffer (10 mM MOPS (sodium salt) (pH 7), 5 mM sodium acetate, 1 mM EDTA). Dried agarose gels were used for direct detection of viral mRNAs by hybridization with a ^{32}P-labeled oligonucleotide probe (5'-CACATGGGGATAGCACTAC-3') that is complementary to a fully conserved sequence located 30 nucleotides upstream of the 3' end of the genome and all subgenomic mRNAs produced by SARS-CoV-2 and SARS-CoV. After hybridization, RNA bands were visualised and quantified by phosphorimaging using a Typhoon-9410 variable mode scanner (GE Healthcare) and ImageQuant TL software (GE Healthcare). In order to verify the amount of RNA loaded, a second hybridization was performed using a ^{32}P-labeled oligonucleotide probe recognizing 18S ribosomal RNA (5'-GATCCGAGGGCCTCACTAAAC-

194 3'). Protein lysates were obtained by lysing infected cell monolayers in 4x Laemmli sample
195 buffer and were analysed by semi-dry Western blotting onto Hybond 0.2µM polyvinylidene
196 difluoride (PVDF) membrane (GE Healthcare). Membranes were incubated with rabbit
197 antisera diluted in PBS with 0.05% Tween-20 containing 5% dry milk (Campina). Primary
198 antibodies were detected with a horseradish peroxidase-conjugated swine anti-rabbit IgG
199 antibody (Dako) and protein bands were visualised using Clarity Western Blot substrate
200 (Biorad) and detected using an Advanced Q9 Alliance imager (Uvitec Cambridge).
201
202 **Next-generation sequencing and bioinformatics analysis**
203 SARS-CoV-2 genomic RNA was isolated from cell culture supernatants using TriPure isolation
204 reagent (Roche Applied Science) and purified according to manufacturer's instructions. The
205 total amount of RNA in samples was measured using a Qubit fluorometer and RNA High
206 Sensitivity kit (Thermo Fisher Scientific). For next-generation sequencing (NGS) library
207 preparation, RNA (25-100 ng) was mixed with random oligonucleotide primers using the
208 NEBNext® First Strand Synthesis Module kit for Illumina® (NEB) and incubated for 10 min at
209 94°C. NGS of samples was performed by a commercial service provider (GenomeScan,
210 Leiden, the Netherlands) while including appropriate quality controls after each step of the
211 procedure. Sequencing was performed using a NovaSeq 6000 Sequencing System (Illumina).
212 Subsequently, sequencing reads were screened for the presence of human (GRCh37.75),
213 mouse (GRCm38.p4), E. coli MG1655 (EMBL U00096.2), phiX (RefSeq NC_001422.1) and
214 common vector sequences (UniVec and ChlSab1.1). Prior to alignment, reads were trimmed
215 to remove adapter sequences and filtered for sequence quality. The remaining reads were
216 mapped to the SARS-CoV-2 GenBank reference sequence (NC_045512.2; (38)). Data
217 analysis was performed using Bowtie 2 (39). Raw NGS data sets for each virus sample
218 analysed in this study are deposited in NCBI Bioproject and available under the following
219 links: ---. Only SARS-CoV-2-specific reads were included in these data files.

To study evolution/adaptation of the S protein gene, we performed an in-depth analysis of reads covering the S1/S2 region of the S protein gene. This was done for the p2 stock and for the four virus samples of the plaque picking experiment shown in Fig. 1a. First, all reads spanning nt 23,576 to 23,665 of the SARS-CoV genome were selected. Next, reads constituting less than 1% of the total number of selected reads were excluded for further analysis. The remaining number of reads were 3,860 (p2 stock), 1,924 (S5p1), 2,263 (S5p2), 4,049 (S5p3) and 3,323 (L8p1). These reads were translated in the S protein open reading frame and the resulting amino acid sequences were aligned, grouped on the basis of containing the same mutations/deletions in the S1/S2 region and ranked by frequency of occurrence (Fig. 1b).

Antisera and immunofluorescence microscopy

The SARS-CoV-specific rabbit or mouse antisera/antibodies used in this study are listed in Table 1. Most antisera were described previously (see references in Table 1), with the exception of three rabbit antisera recognizing SARS-CoV nsps 8, 9 and 15. These were raised using full-length $(His)_6$-tagged bacterial expression products (nsp8 and nsp15) or a synthetic peptide (nsp9, aa 4209-4230 of SARS-CoV pp1a), which were used to immunize New Zealand white rabbits as described previously (40, 41). Cross-reactivity of antisera to SARS-CoV-2 targets was evaluated microscopically by immunofluorescence assay (IFA) and for some antisera (nsp3 and N protein) also by Western blot analysis. Double-stranded RNA was detected using mouse monoclonal antibody J2 from Scicons (42).

Cells were grown on glass coverslips and infected as described above (43). At 12, 24, 48 or 72 h p.i., cells were fixed overnight at 4°C using 3% paraformaldehyde in PBS (pH 7.4). Cells were washed with PBS containing 10 mM glycine and permeabilized with 0.1% Triton X-100 in PBS. Cells were incubated with antisera diluted in PBS containing 5% FCS. Secondary antibodies used were an Alexa488-conjugated goat anti-rabbit IgG antibody (Invitrogen), a Cy3-conjugated donkey anti-rabbit IgG antibody (Jackson ImmunoResearch Laboratories)

and an Alexa488-conjugated goat anti-mouse IgG antibody (Invitrogen). Nuclei were stained with 1 µg/ml Hoechst 33258 (ThermoFischer). Samples were embedded using Prolong Gold (Life Technologies) and analysed with a Leica DM6B fluorescence microscope using LASX software.

Electron microscopy

Vero E6 cells were grown on TC treated Cell Star dishes (Greiner Bio-One) and infected at an m.o.i. of 3, or mock-infected. Cells were fixed after 6, 8 and 10 h p.i. for 30 min at room temperature with freshly prepared 2% (vol/vol) glutaraldehyde in 0.1 M cacodylate buffer (pH 7.4) and then stored overnight in the fixative at 4°C. The samples were then washed with 0.1 M cacodylate buffer, treated for 1 hour with 1% (wt/vol) OsO4 at 4°C, washed with 0.1 M cacodylate buffer and Milli-Q water, and stained with 1% (wt/vol) uranyl acetate in Mili-Q water. After a new washing step, samples were dehydrated in increasing concentrations of ethanol (70%, 80%, 90%,100%), embedded in epoxy resin (LX-112, Ladd Research) and polymerized at 60°C. Sections (100 nm thick) were collected on mesh-100 copper EM grids covered with a carbon-coated Pioloform layer and post-stained with 7% (wt/vol) uranyl acetate and Reynold's lead citrate. The samples were examined in a Twin transmission electron microscope (Thermo Fisher Scientific (formerly FEI)) operated at 120 kV and images were collected with a OneView 4k high-frame rate CMOS camera (Gatan).

Compounds and antiviral screening assay

A 10-mM stock of Remdesivir (HY-104077; MedChemexpress) was dissolved in DMSO and stored in aliquots for single use at -80°C. Alisporivir was kindly provided by DebioPharm (Dr. Grégoire Vuagniaux, Lausanne, Switzerland; (44)) and a 20-mM stock was dissolved in 96% ethanol and stored in aliquots for single use at -20°C. A 20-mM chloroquine stock (C6628; Sigma) was dissolved in PBS and stored in aliquots for single use at -20°C. Pegylated interferon alpha-2a (PEG-IFN-α; Pegasys, 90 mcg, Roche) was aliquoted and stored at room temperature until further use. Vero E6 cells were seeded in a 96-well flat bottom plates in 100

µl at a density of 10,000 cells/well and grown overnight at 37°C. Two-fold serial dilutions of compounds were prepared in EMEM with 2% FCS and 50 µl was added to the cells 30 min prior to infection. Subsequently, half of the wells were infected with 300 PFU each of SARS-CoV or SARS-CoV-2 in order to evaluate inhibition of infection, while the other wells were used to in parallel monitor the (potential) cytotoxicity of compounds. Each compound concentration was tested in quadruplicate and each assay plate contained the following controls: no cells (background control), cells only treated with medium (mock infection for normalization), infected/untreated cells and infected/solvent-treated cells (infection control). At 3 days p.i., 20 µL/well of CellTiter 96 Aqueous Non-Radioactive Cell Proliferation reagent (Promega) was added and plates were incubated for 2 h at 37°C. Reactions were stopped and virus inactivated by adding 30 µl of 37% formaldehyde. Absorbance was measured using a monochromatic filter in a multimode plate reader (Envision; Perkin Elmer). Data was normalized to the mock-infected control, after which EC_{50} and CC_{50} values were calculated with Graph-Pad Prism 7.

RESULTS

Rapid adaptation of SARS-CoV-2 BetaCoV/Australia/VIC01/2020 during passaging in Vero E6 cells

SARS-CoV-2 isolate BetaCoV/Australia/VIC01/2020 was received as a stock derived from two consecutive passages in Vero/hSLAM cells (34). The virus was then propagated two more times at low MOI in Vero E6 cells, in which it caused a severe cytopathic effect (CPE). We also attempted propagation in HuH7 cells, using the same amount of virus or a ten-fold larger inoculum, but did not observe any cytopathology after 72 h (data not shown). At 24 h p.i., immunofluorescence microscopy (see below) revealed infection of only a small percentage of the HuH7 cells, without any clear spread to other cells occurring in the next 48 h. We therefore

conclude that infection of HuH7 cells does not lead to a productive SARS-CoV-2 infection and deemed this cell line unsuitable for further SARS-CoV-2 studies.

The infectivity titre of the Leiden-p2 stock grown in Vero E6 cells was analysed by plaque assay, after which we noticed a mixed plaque phenotype (~1:3 ratio of small versus large (plaques; data not shown) while a virus titre of 7 x 10^6 PFU/ml was calculated. To verify the identity and genome sequence of the SARS-CoV-2/p2 virus stock, we isolated genomic RNA from culture supernatant and applied next-generation sequencing (NGS; see methods for details). The resulting consensus sequence was found to be identical to the sequence previously deposited in GenBank (accession number MT007544.1) (34), with one exception (see below). Compared to the SARS-CoV-2 GenBank reference sequence (NC_045512.3) (38) and other field isolates (29), isolate BetaCoV/Australia/VIC01/2020 exhibits >99.9% sequence identity. In addition to synonymous mutations in the nsp14-coding sequence (U19065 to C) and S protein gene (U22303 to G), ORF3a contains a single non-synonymous mutation (G26144 to U). Strikingly, the 3' untranslated region (UTR) contains a 10-nt deletion (nt 29750-29759; CGAUCGAGUG) located 120 nt upstream of the genomic 3' end , which is not present in other SARS-CoV-2 isolates thus far (>670 SARS-CoV2 sequences present in GenBank on April 17, 2020).

In about 71% of the 95,173 p2 NGS reads covering this position, we noticed a G23607 to A mutation encoding an Arg682 to Gln substitution near the so-called S1/S2 cleavage site of the viral S protein (see Discussion), with the other 29% of the reads being wild-type sequence. As this ratio approximated the observed ratio between large and small plaques, we performed a plaque assay on the p1 virus stock (Fig. 1a, leftmost well) and picked multiple plaques of each size, which were passaged three times in Vero E6 cells while monitoring their plaque phenotype. Interestingly, for several of the small-plaque virus clones (like S5; Fig. 1a) we observed rapid conversion to a mixed or large-plaque phenotype during these three passages, while large-plaque virus clones (like L8) stably retained their plaque phenotype (Fig. 1a). NGS analysis of the genome of a large-plaque p1 virus (L8p1) revealed that >99% of the reads in

329 the S1/S2 cleavage site region contained the G23607 to A mutation described above. No other
330 mutations were detected in the genome, thus clearly linking the Arg682 to Gln substitution in
331 the S protein to the large-plaque phenotype observed for the L8p1 virus.

332 Next, we also analysed the genomes of the p1, p2 and p3 viruses derived from a small-plaque
333 (S5) that was picked. This virus clone retained its small-plaque phenotype during the first
334 passage (Fig. 1a; S5p1), but began to yield an increasing proportion of large(r) plaques during
335 subsequent passages. Sequencing of S5p2 (Fig 1b) revealed a variety of low-frequency reads
336 with mutations near the S1/S2 cleavage site motif (aa 681-687; PRRAR↓SV), with G23607 to
337 A (specifying the Arg682 to Gln substitution) again being the dominant one (in ~0.9% of the
338 reads covering nt 23,576 to 23,665 of the genome). At lower frequencies single-nucleotide
339 changes specifying Arg682 to Trp and Arg683 to Leu substitutions were also detected.
340 Furthermore, a 10-aa deletion (residues 679-688) that erases the S1/S2 cleavage site region
341 was discovered, as well as a 5-aa deletion (residues 675-679) immediately preceding that
342 region. The amount of large plaques increased substantially upon the next passage, with NGS
343 revealing the prominent emergence of the mutants containing the 10-aa deletion or the Arg682
344 to Gln point mutation (~22% and ~12% of the reads, respectively), and yet other minor variants
345 with mutations in the PRRAR↓SV sequence being discovered. Taken together these data
346 clearly link the large-plaque phenotype of SARS-CoV-2 to the acquisition of mutations in this
347 particular region of the S protein, which apparently provides a strong selective advantage
348 during passaging in Vero E6 cells.
349

350 **Comparative kinetics of SARS-CoV and SARS-CoV-2 replication in Vero E6 cells**

351 To our knowledge, a detailed comparison of SARS-CoV-2 and SARS-CoV replication kinetics
352 in cell culture has not been reported so far. Therefore, we infected Vero E6 cells with the
353 SASR-CoV-2/p2 virus stock at high m.o.i. to analyse viral RNA synthesis, protein expression
354 and the release of infectious viral progeny (Fig. 2a). This experiment was performed using 4
355 replicates per time point and for comparison we included the SARS-CoV Frankfurt-1 isolate

(Drosten, Gunther et al. 2003), which has been used in our laboratory since 2003. During the early stages of infection (until 8 h p.i.), the growth curves of the two viruses were similar, but subsequently cells infected with SARS-CoV clearly produced more infectious progeny (about 50-fold more) than SARS-CoV-2-infected cells, with both viruses reaching their plateau by about 14 h p.i. As shown in Fig. 2b, despite its transition to a mainly large-plaque phenotype, the largest SARS-CoV-2/p3 plaques were still substantially smaller than those obtained with SARS-CoV Frankfurt-1.

In parallel, we analysed the kinetics of viral RNA synthesis by isolating intracellular viral RNA, subjecting it to agarose gel electrophoresis and visualizing the various viral mRNA species by in-gel hybridization with a ^{32}P-labeled oligonucleotide probe recognizing a fully conserved 19-nt sequence located 30 nt upstream of the 3' end of both viral genomes (Fig. 3a). This revealed the anticipated presence of the genomic RNA and eight subgenomic mRNAs, together forming the well-known 5'- and 3'- coterminal nested set of transcripts required for full CoV genome expression.

In general, for both viruses, the accumulation of viral RNAs followed the growth curves depicted in Fig. 2a. The relative abundance of the individual RNAs was determined using the 12, 14 and 24 h p.i. samples (averages presented in Fig. 3b) and found to be largely similar, with the exception of SARS-CoV-2 mRNAs 7 and 8, which accumulated to about 4 and 2 times higher levels, respectively. Strikingly, in spite of the ultimately lower yield of infectious viral progeny, SARS-CoV-2 RNA synthesis was detected earlier and reached an overall level exceeding that of SARS-CoV.

We also monitored viral protein production by Western blot analysis using antisera targeting a non-structural (nsp3) and structural (N) protein. As expected from the RNA analysis, the accumulation of both viral proteins increased with time, and was detected somewhat earlier for SARS-CoV-2 than for SARS-CoV (data not shown). Overall, we conclude that in Vero E6 cells, SARS-CoV-2 produces levels of intracellular RNA and proteins that are at least

382 comparable to those of SARS-CoV, although this does not translate into the release of equal
383 amounts of infectious viral progeny (Fig. 2a).

384

385 **Cross-reactivity of antisera previously raised against SARS-CoV targets**

386 To be able to follow virus replication in SARS-CoV-2-infected cells more closely, we explored
387 cross-reactivity of a variety of antisera previously raised against SARS-CoV targets, in
388 particular a variety of nsps. In an earlier study, many of those were found to cross-react also
389 with the corresponding MERS-CoV targets (35), despite the relatively large evolutionary
390 distance between MERS-CoV and SARS-CoV. Based on the much closer relationship with
391 SARS-CoV-2, similar or better cross-reactivity of these SARS-CoV reagents was expected,
392 which was explored using immunofluorescence microscopy.

393 Indeed, most antisera recognizing SARS-CoV nsps that were tested (nsp3, nsp4, nsp5, nsp8,
394 nsp9, nsp13, nsp15) strongly cross-reacted with the corresponding SARS-CoV-2 target (Fig.
395 4 and Table 1), the exception being a polyclonal nsp6 rabbit antiserum. Likewise, both a
396 polyclonal rabbit antiserum and mouse monoclonal antibody recognizing the N protein cross-
397 reacted strongly (Fig. 4b and Table 1). The same was true for a rabbit antiserum raised against
398 a C-terminal peptide of the SARS-CoV M protein (Fig 4e). Labelling patterns were essentially
399 identical to those previously documented for SARS-CoV (Stertz, Reichelt et al. 2007, Knoops,
400 Kikkert et al. 2008), with nsps accumulating in the perinuclear region of infected cells, where
401 the elaborate membrane structures of the viral ROs are formed (Fig. 4a, c, d). Punctate
402 structures in the same area of the cell were labelled using an antibody recognizing double-
403 stranded RNA (dsRNA), which presumably recognizes replicative intermediates of viral RNA
404 synthesis (45, 46). The N protein signal was diffusely cytosolic (Fig. 4b), whereas the M protein
405 labelling predominantly showed the expected localization to the Golgi complex (Fig. 4e), where
406 the protein is known to accumulate (47).

407

408

Ultrastructural characterisation of SARS-CoV-2-infected cells

We next used electron microscopy to investigate the ultrastructural changes that SARS-CoV-2 induces in infected cells, and focused on the membranous replication organelles (ROs) that supports viral RNA synthesis and on the assembly and release of new virions (Fig. 5). Compared to mock-infected control cells (Fig. 5a-b), various distinct membrane alterations were observed in cells infected with either SARS-CoV or SARS-CoV-2 (Fig. 5c-j). At 6 h p.i., larger regions with membrane alterations were found particularly in cells infected with SARS-CoV-2 (data not shown), which may align with the somewhat faster onset of intracellular RNA synthesis in SARS-CoV2-infected Vero E6 cells (Fig. 3a). From 8 h p.i onwards, SARS-CoV- and SARS-CoV-2-infected cells appeared more similar (Fig. 5c-f and 5g-j). Double-membrane vesicles (DMVs) were the most prominent membrane alteration up to this stage (Fig. 5d-e and and 5h-i, asterisks). In addition, convoluted membranes (45) were readily detected in SARS-CoV-infected cells, while zippered ER (25, 48, 49) appeared to be the predominant structure in SARS-CoV-2-infected cells (Fig. 5e and 5i, white arrowheads). As previously described for SARS-CoV (45), also SARS-CoV-2-induced DMV appeared to fuse through their outer membrane, giving rise to vesicles packets that increased in numbers as infection progressed (Fig 5f and 5k, white asterisks). Virus budding near the Golgi apparatus, presumably into smooth membranes of the ER-Golgi intermediate compartment (ERGIC) (50-52), was frequently observed at 8 h p.i. (Fig. 5k-l and 5o-p). This step is followed by transport to the plasma membrane and release of virus particles into extracellular space. By 10 h p.i., released progeny virions were abundantly detected around all infected cells (Fig. 5m-n and 5q-r). Interestingly, whereas spikes were clearly present on SARS-CoV progeny virions, a relatively large proportion of SARS-CoV-2 particles seemed to carry few or no visible spike projections on their surface, perhaps suggesting a relatively inefficient incorporation of spike proteins into SARS-CoV-2 virions. This could potentially reduce the yield of infectious particles and may contribute to the lower progeny titres obtained for this virus (Fig. 2a).

437 **Establishing a CPE-based assay to screen compounds for anti-SARS-CoV-2 activity**

438 In order to establish and validate a CPE-based assay to identify potential inhibitors of SARS-
439 CoV-2 replication, we selected four previously identified inhibitors of CoV replication:
440 Remdesivir (53, 54), chloroquine (55, 56), Alisporivir (57, 58) and pegylated interferon alpha
441 (PEG-IFN-α) (35, 59). Cells were infected at low MOI to allow for multiple cycles of replication.
442 After three days, a colorimetric cell viability assay (60) was used to measure drug toxicity and
443 inhibition of virus replication in mock- and virus-infected cells, respectively. With the exception
444 of PEG-IFN-α, the inhibition of virus replication by compounds tested and the calculated half-
445 maximal effective concentrations (EC_{50}) were similar for SARS-CoV and SARS-CoV-2. For
446 Remdesivir, we obtained higher EC_{50} values for SARS-CoV-2 and SARS-CoV (4.4 and 4.5
447 µM, respectively; Fig. 6a) than previously reported by others, but this may be explained by
448 technical differences like a longer assay incubation time (72 h instead of 48 h) and the use of
449 a different read-out (cell viability instead of qRT-PCR or viral load). Based on the obtained
450 CC_{50} values of >100 µM, a selectivity index >22.5 was calculated. Chloroquine potently
451 blocked virus infection at low-micromolar concentrations, with an EC_{50} value of 2.3 µM for both
452 viruses (CC_{50} >100 µM, SI >45.5; Fig. 6b). Alisporivir, a known inhibitor of different groups of
453 RNA viruses, was previously found to effectively reduce the production of CoV progeny. In
454 this study, we measured EC_{50} values of 4.9 and 4.3 µM for SARS-CoV-2 and SARS-CoV,
455 respectively (Fig. 6c; CC_{50}>100 µM, SI >20). Treatment with PEG-IFN-α completely inhibited
456 replication of SARS-CoV-2, even at the lowest dose of 7.8 ng/ml (Fig. 6d). In line with previous
457 results (35, 59), SARS-CoV was much less sensitive to PEG-IFN-α treatment, yielding only
458 partial inhibition at all concentrations tested (from 7.8 to 1000 ng/ml). Overall, we conclude
459 that Vero E6 cells provide a suitable basis to perform antiviral compound screening and select
460 the most promising hits for in-depth mechanistic studies and further development.
461

Discussion

In this report, we describe a comparative analysis of the replication features of SARS-CoV-2 and SARS-CoV in Vero E6 cells, one of the most commonly used cell lines for studying these two viruses. However, in contrast to the stable phenotype exhibited by SARS-CoV during our 17 years of working with this virus in these cells, SARS-CoV-2 began to exhibit remarkable phenotypic variation in plaque assays within a few passages after its isolation from clinical samples (Fig. 1a). In addition to the BetaCoV/Australia/VIC01/2020 isolate used in this study, similar observations were made for a variety of other clinical isolates (data not shown). To establish the genetic basis for the observed plaque size heterogeneity, small and large plaques were picked and the resulting virus clones were passaged repeatedly and analysed using NGS. The consensus sequences obtained for S5p1 and L8p1, which differed by a single nucleotide substitution in the S protein gene, clearly established that a single S protein mutation (Arg682 to Gln) was responsible for the observed plaque size difference. This mutation is localized near the so-called 'furin-like' S1/S2 cleavage site (Fig. 1b) (61) in the S protein (62). This sequence constitutes a (potential) processing site that is present in a subset of CoVs (including SARS-CoV-2 and MERS-CoV) but is lacking in others, like SARS-CoV and certain bat CoVs (61, 63). This polybasic motif (PRRAR↓SV, in SARS-CoV-2) can be recognized by intracellular furin-like proteases during viral egress and its cleavage is thought to prime the S protein for fusion and entry (64), which also requires a second cleavage event to occur at the downstream S2' cleavage site (61). In general, the presence of the furin-like cleavage site does not appear to be critical for successful CoV infection. Using pseudotyped virions carrying mutant S proteins of SARS-CoV (65) or SARS-CoV-2 (66), it was shown that its presence minimally impacts S protein functionality. In the SARS-CoV S protein, an adjacent sequence that is conserved across CoVs can be cleaved by other host proteases like cathepsin L or TMPRSS2 (67-69), thus providing an alternative pathway to trigger viral entry. Possibly, this pathway is also employed by our Vero E6-cell adapted SARS-CoV-2 mutants that have lost the furin-like cleavage site, like clone L8p1 and multiple variants encountered in

S5p3 (Fig. 1a). These variants contain either single point mutations or deletions of 5 to 10 aa (Fig. 1b), resembling variants recently reported by other laboratories (30, 70, 71). Interestingly similar changes were also observed in some clinical SARS-CoV-2 isolates that had not been passaged in cell culture (70). It is currently being investigated why mutations that inactivate the furin-like cleavage site provide such a major selective advantage during SARS-CoV-2 passaging in Vero E6 cells and how this translates into the striking large-plaque phenotype documented in this paper.

An additional remarkable feature confirmed by our re-sequencing of the BetaCoV/Australia/VIC01/2020 isolate of SARS-CoV-2 is the presence of a 10-nt deletion in the 3' UTR of the genome (34). Screening of other available SARS-CoV-2 genome sequences indicated that the presence of this deletion apparently is unique for this particular isolate, and likely represents an additional adaptation acquired during cell culture passaging. This deletion maps to a previously described "hypervariable region" in the otherwise conserved 3' UTR, and in particular to the so-called s2m motif (72) that is conserved among CoVs and also found in several other virus groups (73, 74). The s2m element has been implicated in the binding of host factors to viral RNAs, but its exact function has remained enigmatic thus far. Strikingly, for the mouse hepatitis coronavirus the entire hypervariable region (including s2m) was found to be dispensable for replication in cell culture, but highly relevant for viral pathogenesis in mice (72). Although the impact of this deletion for SARS-CoV-2 remains to be studied in more detail, these previous data suggest that this mutation need not have a major impact on SARS-CoV-2 replication in Vero E6 cells. This notion is also supported by the fact that the results of our antiviral screening assays (Fig. 6) correlate well with similar studies performed with other SARS-CoV-2 isolates (54, 75, 76). Clearly, this could be different for *in vivo* studies, for which it would probably be better to rely on SARS-CoV-2 isolates not carrying this deletion in their 3' UTR.

Vero E6 cells are commonly used to isolate, propagate, and study SARS-CoV-like viruses as they support viral replication to high titres (77-81). This may be due to a high expression level

of the ACE-2 receptor (82) that is used by both SARS-CoV-2 and SARS-CoV (9) and/or the fact that they lack the ability to produce interferon (83, 84). It will be interesting to evaluate whether there is a similarly strong selection pressure to adapt the S1/S2 region of the S protein when SARS-CoV-2 is passaged in other cell types. Such studies are currently in progress in our laboratory and already established that HuH7 cells may be a poor choice, despite the fact that they were used for virus propagation (9, 85) and antiviral screening in other studies (54, 86). Immunolabelling of infected HuH7 cells (data not shown) revealed non-productive infection of only a small fraction of the cells and a general lack of cytopathology. While other cell lines are being evaluated, as illustrated above, the monitoring of the plaque phenotype (plaque size and homogeneity) may provide a quick and convenient method to assess the composition of SARS-CoV-2 stocks propagated in Vero E6 cells, at least where it concerns the evolution of the S1/S2 region of the S protein.

Given the ongoing SARS-CoV-2 pandemic, the detailed characterization of its replication cycle is an important step in understanding the molecular biology of the virus and defining potential targets for inhibitors of replication. The cross-reacting antisera described in this study (Table 1) will be a useful tool during such studies. In general, the subcellular localization of viral nsps and structural proteins (Fig. 4) and the ultrastructural changes associated with RO formation (Fig. 5) were very similar for the two viruses. We also observed comparable replication kinetics for SARS-CoV-2 and SARS-CoV in Vero E6 cells, although clearly lower final infectivity titres were measured for SARS-CoV-2 (~50-fold lower; Fig. 2). Nevertheless, RNA synthesis could be detected somewhat earlier for SARS-CoV-2 and the overall amount of viral RNA produced exceeded that produced by SARS-CoV (Fig. 3). This may be indicative of certain assembly or maturation problems or of virus-host interactions that are different in the case SARS-CoV-2. These possibilities merit further investigation, in particular since our preliminary EM studies suggested intriguing differences with SARS-CoV where it concerns the presence of spikes on the surface of freshly released SARS-CoV-2 particles (Fig. 5n and 5r).

543 Our analysis of SARS-CoV-2 subgenomic mRNA synthesis revealed the increased relative
544 abundance of mRNAs 7 and 8 (~4- and ~2-fold, respectively) when SARS-CoV-2 was
545 compared to SARS-CoV. Mechanistically, these differences do not appear to be caused by
546 extended base pairing possibilities of the transcription regulatory sequences that direct the
547 synthesis of these two mRNAs (24). As in SARS-CoV, mRNA7 of SARS-CoV-2 encodes for
548 two proteins, the ORF7a and ORF7b proteins, with the latter presumably being expressed
549 following leaky ribosomal scanning (32). Upon its ectopic expression, the ORF7a protein has
550 been reported to induce apoptosis via a caspase-dependent pathway (87) and/or to be
551 involved in cell cycle arrest (88). The ORF7b product is a poorly studied integral membrane
552 protein that has (also) been detected in virions (89). When ORF7a/b or ORF7a were deleted
553 from the SARS-CoV genome, there was a minimal impact on the kinetics of virus replication
554 *in vitro* in different cell lines, including Vero cells, and *in vivo* using mice. In another study,
555 however, partial deletion of SARS-CoV ORF7b was reported to provide a replicative
556 advantage in CaCo-2 and HuH7 cells, but not in Vero cells (90).

557 The SARS-CoV ORF8 protein is membrane-associated and able to induce endoplasmic
558 reticulum stress (91, 92), although it has not been characterised in great detail in the context
559 of viral infection. Soon after the emergence of SARS-CoV in 2003, a conspicuous 29-nt (out-
560 of-frame) deletion in ORF8 was noticed in late(r) human isolates, but not in early human
561 isolates and SARS-like viruses obtained from animal sources (93-95). Consequently, loss of
562 ORF8 function was postulated to reflect an adaptation to the human host. The re-engineering
563 of an intact ORF8, using a reverse genetics system for the SARS-CoV Frankfurt-1 isolate,
564 yielded a virus with strikingly enhanced (up to 23-fold) replication properties in multiple
565 systems (96) . Clearly, it remains to be established that the increased synthesis of mRNAs 7
566 and 8 is a general feature of SARS-CoV-2 isolates, and that this indeed also translates into
567 higher expression levels of the accessory proteins encoded by ORFs 7a, 7b and 8. If
568 confirmed, these differences definitely warrant an in-depth follow-up analysis as CoV
569 accessory proteins in general have been shown to be important determinants of virulence.

570 They may thus be relevant for our understanding of the wide spectrum of respiratory disease
571 symptoms observed in COVID-19 patients (97).

572 Based on the close ancestral relationship between SARS-CoV-2 and SARS-CoV (98), one
573 might expect that the patterns and modes of interaction with host antiviral defence
574 mechanisms would be similar. However, our experiments with type I interferon treatment of
575 Vero E6 cells (Fig. 6) revealed a clear difference, with SARS-CoV-2 being considerably more
576 sensitive than SARS-CoV, as also observed by other laboratories (76). Essentially, SARS-
577 CoV-2 replication could be inhibited by similarly low concentrations of PEG-IFN-alpha-2a that
578 inhibit MERS-CoV replication in cell culture (35). Taken together, our data suggest that SARS-
579 CoV-2 is less able to counter a primed type I IFN response than SARS-CoV (76, 99).

580 Previously identified inhibitors of CoV replication were used to further validate our cell-based
581 assay for SARS-CoV-2 inhibitor screening. These compounds inhibited replication at similar
582 low-micromolar concentrations and in a similar dose-dependent manner as observed for
583 SARS-CoV (Fig. 6). Remdesivir is a prodrug of an adenosine analogue developed by Gilead
584 Sciences. It was demonstrated to target the CoV RNA polymerase and act as a chain
585 terminator (100-102). The clinical efficacy of Remdesivir is still being evaluated and, after
586 some first encouraging results (103), worldwide compassionate use trials are now being
587 conducted. Likewise, hydroxychloroquine and chloroquine have been labelled as potential
588 “game changers” and are being evaluated for treatment of severe COVID-19 patients (104).
589 Both compounds have been used to treat malaria and amebiasis (105), until drug-resistant
590 *Plasmodium* strains emerged (106). These compounds can be incorporated into endosomes
591 and lysosomes, raising the pH inside these intracellular compartments, which in turn may lead
592 to defects in protein degradation and intracellular trafficking (68, 107). An alternative
593 hypothesis to explain their anti-SARS-CoV activity is based on their impact on glycosylation
594 of the ACE2 receptor that is used by SARS-CoV (56). Finally, as expected, the non-
595 immunosuppressive cyclosporin A analogue Alisporivir inhibited SARS-CoV-2 replication, as
596 demonstrated previously for SARS-CoV and MERS-CoV (58). Although the exact mode of

597 action of this inhibitor it is unclear, it is thought to modulate CoV interactions with members of
598 the cyclophilin family (108). Unfortunately, all of these *in vitro* antiviral activities should
599 probably be classified as modest, emphasizing the urgency of large-scale drug repurposing
600 and discovery programmes that target SARS-CoV-2 and coronaviruses at large.

Authors and contributors

NO, JD, MK, MB, IS and ES conceptualised the study. NO, TD, JZ, RL, YM and LC performed experimental work and contributed to analysis of the results and preparation of figures. NO, LC, JD, JV, IS and ES performed NGS and were involved in the bioinformatics analysis of the data. NO and ES wrote the manuscript, with input from all authors.

Conflicts of interest:

The authors declare that there are no conflicts of interest.

Funding information:

None.

Acknowledgements:

We thank various GenomeScan staff members for the pleasant and swift collaboration that facilitated the NGS and data analysis of the first SARS-CoV-2 samples. We are grateful to all members of the sections Research and Clinical Microbiology of the LUMC Department of Medical Microbiology for their collaborative support and dedication during the current pandemic situation. In particular, we thank Linda Boomaars, Peter Bredenbeek, Ien Dobbelaar, Martijn van Hemert, Sebenzile Myeni, Tessa Nelemans, Esther Quakkelaar, Ali Tas, Tessa Nelemans, Sjaak Voorden and Gijsbert van Willigen for their technical or administrative support, constructive discussions and/or scientific input.

REFERENCES

1. Coronaviridae Study Group of the International Committee on Taxonomy of V. The species Severe acute respiratory syndrome-related coronavirus: classifying 2019-nCoV and naming it SARS-CoV-2. Nat Microbiol. 2020;5(4):536-44.
2. Li X, Song Y, Wong G, Cui J. Bat origin of a new human coronavirus: there and back again. Sci China Life Sci. 2020;63(3):461-2.
3. McIntosh K, Chao RK, Krause HE, Wasil R, Mocega HE, Mufson MA. Coronavirus infection in acute lower respiratory tract disease of infants. J Infect Dis. 1974;130(5):502-7.
4. Pyrc K, Berkhout B, van der Hoek L. Identification of new human coronaviruses. Expert Rev Anti Infect Ther. 2007;5(2):245-53.
5. Ksiazek TG, Erdman D, Goldsmith CS, Zaki SR, Peret T, Emery S, et al. A novel coronavirus associated with severe acute respiratory syndrome. N Engl J Med. 2003;348(20):1953-66.
6. Peiris JS, Lai ST, Poon LL, Guan Y, Yam LY, Lim W, et al. Coronavirus as a possible cause of severe acute respiratory syndrome. Lancet. 2003;361(9366):1319-25.
7. Zaki AM, van Boheemen S, Bestebroer TM, Osterhaus AD, Fouchier RA. Isolation of a novel coronavirus from a man with pneumonia in Saudi Arabia. N Engl J Med. 2012;367(19):1814-20.
8. van Boheemen S, de Graaf M, Lauber C, Bestebroer TM, Raj VS, Zaki AM, et al. Genomic characterization of a newly discovered coronavirus associated with acute respiratory distress syndrome in humans. mBio. 2012;3(6).
9. Zhou P, Yang XL, Wang XG, Hu B, Zhang L, Zhang W, et al. A pneumonia outbreak associated with a new coronavirus of probable bat origin. Nature. 2020;579(7798):270-3.
10. Munster VJ, Koopmans M, van Doremalen N, van Riel D, de Wit E. A Novel Coronavirus Emerging in China - Key Questions for Impact Assessment. N Engl J Med. 2020;382(8):692-4.
11. Li X, Zai J, Zhao Q, Nie Q, Li Y, Foley BT, et al. Evolutionary history, potential intermediate animal host, and cross-species analyses of SARS-CoV-2. J Med Virol. 2020.
12. Lam TT, Shum MH, Zhu HC, Tong YG, Ni XB, Liao YS, et al. Identifying SARS-CoV-2 related coronaviruses in Malayan pangolins. Nature. 2020.
13. Andersen KG, Rambaut A, Lipkin WI, Holmes EC, Garry RF. The proximal origin of SARS-CoV-2. Nature Medicine. 2020.
14. Song HD, Tu CC, Zhang GW, Wang SY, Zheng K, Lei LC, et al. Cross-host evolution of severe acute respiratory syndrome coronavirus in palm civet and human. Proc Natl Acad Sci U S A. 2005;102(7):2430-5.
15. Reusken CB, Haagmans BL, Muller MA, Gutierrez C, Godeke GJ, Meyer B, et al. Middle East respiratory syndrome coronavirus neutralising serum antibodies in dromedary camels: a comparative serological study. Lancet Infect Dis. 2013;13(10):859-66.
16. Ge XY, Li JL, Yang XL, Chmura AA, Zhu G, Epstein JH, et al. Isolation and characterization of a bat SARS-like coronavirus that uses the ACE2 receptor. Nature. 2013;503(7477):535-8.
17. Menachery VD, Yount BL, Jr., Debbink K, Agnihothram S, Gralinski LE, Plante JA, et al. A SARS-like cluster of circulating bat coronaviruses shows potential for human emergence. Nat Med. 2015;21(12):1508-13.
18. Hu B, Zeng LP, Yang XL, Ge XY, Zhang W, Li B, et al. Discovery of a rich gene pool of bat SARS-related coronaviruses provides new insights into the origin of SARS coronavirus. PLoS Pathog. 2017;13(11):e1006698.
19. Cui J, Li F, Shi ZL. Origin and evolution of pathogenic coronaviruses. Nat Rev Microbiol. 2019;17(3):181-92.

20. Corman VM, Baldwin HJ, Tateno AF, Zerbinati RM, Annan A, Owusu M, et al. Evidence for an Ancestral Association of Human Coronavirus 229E with Bats. J Virol. 2015;89(23):11858-70.
21. Li W, Hulswit RJG, Kenney SP, Widjaja I, Jung K, Alhamo MA, et al. Broad receptor engagement of an emerging global coronavirus may potentiate its diverse cross-species transmissibility. Proc Natl Acad Sci U S A. 2018;115(22):E5135-E43.
22. Zhou P, Fan H, Lan T, Yang XL, Shi WF, Zhang W, et al. Fatal swine acute diarrhoea syndrome caused by an HKU2-related coronavirus of bat origin. Nature. 2018;556(7700):255-8.
23. Nga PT, Parquet Mdel C, Lauber C, Parida M, Nabeshima T, Yu F, et al. Discovery of the first insect nidovirus, a missing evolutionary link in the emergence of the largest RNA virus genomes. PLoS Pathog. 2011;7(9):e1002215.
24. Snijder EJ, Decroly E, Ziebuhr J. The Nonstructural Proteins Directing Coronavirus RNA Synthesis and Processing. Adv Virus Res. 2016;96:59-126.
25. Snijder EJ, Limpens RWAL, de Wilde AH, de Jong AWM, Zevenhoven-Dobbe JC, Maier HJ, et al. A unifying structural and functional model of the coronavirus replication organelle: tracking down RNA synthesis. bioRxiv. 2020.
26. Narayanan K, Huang C, Makino S. SARS coronavirus accessory proteins. Virus Res. 2008;133(1):113-21.
27. Li G, De Clercq E. Therapeutic options for the 2019 novel coronavirus (2019-nCoV). Nat Rev Drug Discov. 2020;19(3):149-50.
28. Ogando NS, Ferron F, Decroly E, Canard B, Posthuma CC, Snijder EJ. The Curious Case of the Nidovirus Exoribonuclease: Its Role in RNA Synthesis and Replication Fidelity. Front Microbiol. 2019;10:1813.
29. Lu R, Zhao X, Li J, Niu P, Yang B, Wu H, et al. Genomic characterisation and epidemiology of 2019 novel coronavirus: implications for virus origins and receptor binding. Lancet. 2020;395(10224):565-74.
30. Wu F, Zhao S, Yu B, Chen YM, Wang W, Song ZG, et al. A new coronavirus associated with human respiratory disease in China. Nature. 2020;579(7798):265-9.
31. Hoffmann M, Kleine-Weber H, Krüger N, Müller M, Drosten C, Pöhlmann S. The novel coronavirus 2019 (2019-nCoV) uses the SARS-coronavirus receptor ACE2 and the cellular protease TMPRSS2 for entry into target cells. bioRxiv. 2020.
32. Snijder EJ, Bredenbeek PJ, Dobbe JC, Thiel V, Ziebuhr J, Poon LL, et al. Unique and conserved features of genome and proteome of SARS-coronavirus, an early split-off from the coronavirus group 2 lineage. J Mol Biol. 2003;331(5):991-1004.
33. Thiel V, Ivanov KA, Putics A, Hertzig T, Schelle B, Bayer S, et al. Mechanisms and enzymes involved in SARS coronavirus genome expression. J Gen Virol. 2003;84(Pt 9):2305-15.
34. Caly L DJ, Roberts J, Bond K, Tran T, Kostecki R, Yoga Y, Naughton W, Taiaroa G, Seemann T, Schultz, Howden B, Korman T, Lewin S, Williamson D, Catton M. Isolation and rapid sharing of the 2019 novel coronavirus (SAR-CoV-2) from the first diagnosis of COVID-19 in Australia. the medical journal of australia. 2020.
35. de Wilde AH, Raj VS, Oudshoorn D, Bestebroer TM, van Nieuwkoop S, Limpens R, et al. MERS-coronavirus replication induces severe in vitro cytopathology and is strongly inhibited by cyclosporin A or interferon-alpha treatment. J Gen Virol. 2013;94(Pt 8):1749-60.
36. Drosten C, Gunther S, Preiser W, van der Werf S, Brodt HR, Becker S, et al. Identification of a novel coronavirus in patients with severe acute respiratory syndrome. N Engl J Med. 2003;348(20):1967-76.
37. van den Worm SH, Eriksson KK, Zevenhoven JC, Weber F, Zust R, Kuri T, et al. Reverse genetics of SARS-related coronavirus using vaccinia virus-based recombination. PLoS One. 2012;7(3):e32857.
38. Wu F, Zhao S, Yu B, Chen Y-M, Wang W, Hu Y, et al. Complete genome characterisation of a novel coronavirus associated with severe human respiratory disease in Wuhan, China. bioRxiv. 2020.

39. Langmead B, Salzberg SL. Fast gapped-read alignment with Bowtie 2. Nat Methods. 2012;9(4):357-9.
40. Snijder EJ, Wassenaar AL, Spaan WJ. Proteolytic processing of the replicase ORF1a protein of equine arteritis virus. J Virol. 1994;68(9):5755-64.
41. Fang Y, Pekosz A, Haynes L, Nelson EA, Rowland RR. Production and characterization of monoclonal antibodies against the nucleocapsid protein of SARS-CoV. Adv Exp Med Biol. 2006;581:153-6.
42. Schonborn J, Oberstrass J, Breyel E, Tittgen J, Schumacher J, Lukacs N. Monoclonal antibodies to double-stranded RNA as probes of RNA structure in crude nucleic acid extracts. Nucleic Acids Res. 1991;19(11):2993-3000.
43. van der Meer Y, Snijder EJ, Dobbe JC, Schleich S, Denison MR, Spaan WJ, et al. Localization of mouse hepatitis virus nonstructural proteins and RNA synthesis indicates a role for late endosomes in viral replication. J Virol. 1999;73(9):7641-57.
44. Coelmont L, Kaptein S, Paeshuyse J, Vliegen I, Dumont JM, Vuagniaux G, et al. Debio 025, a cyclophilin binding molecule, is highly efficient in clearing hepatitis C virus (HCV) replicon-containing cells when used alone or in combination with specifically targeted antiviral therapy for HCV (STAT-C) inhibitors. Antimicrob Agents Chemother. 2009;53(3):967-76.
45. Knoops K, Kikkert M, Worm SH, Zevenhoven-Dobbe JC, van der Meer Y, Koster AJ, et al. SARS-coronavirus replication is supported by a reticulovesicular network of modified endoplasmic reticulum. PLoS Biol. 2008;6(9):e226.
46. Weber F, Wagner V, Rasmussen SB, Hartmann R, Paludan SR. Double-stranded RNA is produced by positive-strand RNA viruses and DNA viruses but not in detectable amounts by negative-strand RNA viruses. J Virol. 2006;80(10):5059-64.
47. Snijder EJ, van der Meer Y, Zevenhoven-Dobbe J, Onderwater JJ, van der Meulen J, Koerten HK, et al. Ultrastructure and origin of membrane vesicles associated with the severe acute respiratory syndrome coronavirus replication complex. J Virol. 2006;80(12):5927-40.
48. Maier HJ, Hawes PC, Cottam EM, Mantell J, Verkade P, Monaghan P, et al. Infectious bronchitis virus generates spherules from zippered endoplasmic reticulum membranes. mBio. 2013;4(5):e00801-13.
49. Doyle N, Hawes PC, Simpson J, Adams LH, Maier HJ. The Porcine Deltacoronavirus Replication Organelle Comprises Double-Membrane Vesicles and Zippered Endoplasmic Reticulum with Double-Membrane Spherules. Viruses. 2019;11(11).
50. Tooze J, Tooze S, Warren G. Replication of coronavirus MHV-A59 in sac- cells: determination of the first site of budding of progeny virions. Eur J Cell Biol. 1984;33(2):281-93.
51. Goldsmith CS, Tatti KM, Ksiazek TG, Rollin PE, Comer JA, Lee WW, et al. Ultrastructural characterization of SARS coronavirus. Emerg Infect Dis. 2004;10(2):320-6.
52. Stertz S, Reichelt M, Spiegel M, Kuri T, Martinez-Sobrido L, Garcia-Sastre A, et al. The intracellular sites of early replication and budding of SARS-coronavirus. Virology. 2007;361(2):304-15.
53. Agostini ML, Andres EL, Sims AC, Graham RL, Sheahan TP, Lu X, et al. Coronavirus Susceptibility to the Antiviral Remdesivir (GS-5734) Is Mediated by the Viral Polymerase and the Proofreading Exoribonuclease. mBio. 2018;9(2).
54. Wang M, Cao R, Zhang L, Yang X, Liu J, Xu M, et al. Remdesivir and chloroquine effectively inhibit the recently emerged novel coronavirus (2019-nCoV) in vitro. Cell Res. 2020;30(3):269-71.
55. Keyaerts E, Vijgen L, Maes P, Neyts J, Van Ranst M. In vitro inhibition of severe acute respiratory syndrome coronavirus by chloroquine. Biochem Biophys Res Commun. 2004;323(1):264-8.
56. Vincent MJ, Bergeron E, Benjannet S, Erickson BR, Rollin PE, Ksiazek TG, et al. Chloroquine is a potent inhibitor of SARS coronavirus infection and spread. Virol J. 2005;2:69.

57. Carbajo-Lozoya J, Ma-Lauer Y, Malesevic M, Theuerkorn M, Kahlert V, Prell E, et al. Human coronavirus NL63 replication is cyclophilin A-dependent and inhibited by non-immunosuppressive cyclosporine A-derivatives including Alisporivir. Virus Res. 2014;184:44-53.
58. de Wilde AH, Falzarano D, Zevenhoven-Dobbe JC, Beugeling C, Fett C, Martellaro C, et al. Alisporivir inhibits MERS- and SARS-coronavirus replication in cell culture, but not SARS-coronavirus infection in a mouse model. Virus Res. 2017;228:7-13.
59. Haagmans BL, Kuiken T, Martina BE, Fouchier RA, Rimmelzwaan GF, van Amerongen G, et al. Pegylated interferon-alpha protects type 1 pneumocytes against SARS coronavirus infection in macaques. Nat Med. 2004;10(3):290-3.
60. Riss TL, Moravec RA, Niles AL, Duellman S, Benink HA, Worzella TJ, et al. Cell Viability Assays. In: Sittampalam GS, Grossman A, Brimacombe K, Arkin M, Auld D, Austin CP, et al., editors. Assay Guidance Manual. Bethesda (MD)2004.
61. Coutard B, Valle C, de Lamballerie X, Canard B, Seidah NG, Decroly E. The spike glycoprotein of the new coronavirus 2019-nCoV contains a furin-like cleavage site absent in CoV of the same clade. Antiviral Res. 2020;176:104742.
62. Izaguirre G. The Proteolytic Regulation of Virus Cell Entry by Furin and Other Proprotein Convertases. Viruses. 2019;11(9).
63. Zhou P, Yang X-L, Wang X-G, Hu B, Zhang L, Zhang W, et al. Discovery of a novel coronavirus associated with the recent pneumonia outbreak in humans and its potential bat origin. bioRxiv. 2020.
64. Millet JK, Whittaker GR. Host cell entry of Middle East respiratory syndrome coronavirus after two-step, furin-mediated activation of the spike protein. Proc Natl Acad Sci U S A. 2014;111(42):15214-9.
65. Follis KE, York J, Nunberg JH. Furin cleavage of the SARS coronavirus spike glycoprotein enhances cell-cell fusion but does not affect virion entry. Virology. 2006;350(2):358-69.
66. Walls AC, Park YJ, Tortorici MA, Wall A, McGuire AT, Veesler D. Structure, Function, and Antigenicity of the SARS-CoV-2 Spike Glycoprotein. Cell. 2020;181(2):281-92 e6.
67. Bosch BJ, Bartelink W, Rottier PJ. Cathepsin L functionally cleaves the severe acute respiratory syndrome coronavirus class I fusion protein upstream of rather than adjacent to the fusion peptide. J Virol. 2008;82(17):8887-90.
68. Burkard C, Verheije MH, Wicht O, van Kasteren SI, van Kuppeveld FJ, Haagmans BL, et al. Coronavirus cell entry occurs through the endo-/lysosomal pathway in a proteolysis-dependent manner. PLoS Pathog. 2014;10(11):e1004502.
69. Huang IC, Bosch BJ, Li F, Li W, Lee KH, Ghiran S, et al. SARS coronavirus, but not human coronavirus NL63, utilizes cathepsin L to infect ACE2-expressing cells. J Biol Chem. 2006;281(6):3198-203.
70. Liu Z, Zheng H, Yuan R, Li M, Lin H, Peng J, et al. Identification of a common deletion in the spike protein of SARS-CoV-2. bioRxiv. 2020.
71. Davidson AD, Williamson MK, Lewis S, Shoemark D, Carroll MW, Heesom K, et al. Characterisation of the transcriptome and proteome of SARS-CoV-2 using direct RNA sequencing and tandem mass spectrometry reveals evidence for a cell passage induced in-frame deletion in the spike glycoprotein that removes the furin-like cleavage site. bioRxiv. 2020.
72. Goebel SJ, Miller TB, Bennett CJ, Bernard KA, Masters PS. A hypervariable region within the 3' cis-acting element of the murine coronavirus genome is nonessential for RNA synthesis but affects pathogenesis. J Virol. 2007;81(3):1274-87.
73. Stammler SN, Cao S, Chen SJ, Giedroc DP. A conserved RNA pseudoknot in a putative molecular switch domain of the 3'-untranslated region of coronaviruses is only marginally stable. RNA. 2011;17(9):1747-59.
74. Rangan R, Zheludev IN, Das R. RNA genome conservation and secondary structure in SARS-CoV-2 and SARS-related viruses. bioRxiv. 2020.

75. Choy KT, Wong AY, Kaewpreedee P, Sia SF, Chen D, Hui KPY, et al. Remdesivir, lopinavir, emetine, and homoharringtonine inhibit SARS-CoV-2 replication in vitro. Antiviral Res. 2020;178:104786.
76. Lokugamage KG, Schindewolf C, Menachery VD. SARS-CoV-2 sensitive to type I interferon pretreatment. bioRxiv. 2020.
77. Banerjee A, Nasir JA, Budylowski P, Yip L, Aftanas P, Christie N, et al. Isolation, sequence, infectivity and replication kinetics of SARS-CoV-2. bioRxiv. 2020.
78. Matsuyama S, Nao N, Shirato K, Kawase M, Saito S, Takayama I, et al. Enhanced isolation of SARS-CoV-2 by TMPRSS2-expressing cells. Proc Natl Acad Sci U S A. 2020.
79. Tseng CT, Tseng J, Perrone L, Worthy M, Popov V, Peters CJ. Apical entry and release of severe acute respiratory syndrome-associated coronavirus in polarized Calu-3 lung epithelial cells. J Virol. 2005;79(15):9470-9.
80. Mossel EC, Huang C, Narayanan K, Makino S, Tesh RB, Peters CJ. Exogenous ACE2 expression allows refractory cell lines to support severe acute respiratory syndrome coronavirus replication. J Virol. 2005;79(6):3846-50.
81. Kaye M. SARS-associated coronavirus replication in cell lines. Emerg Infect Dis. 2006;12(1):128-33.
82. Gillim-Ross L, Taylor J, Scholl DR, Ridenour J, Masters PS, Wentworth DE. Discovery of novel human and animal cells infected by the severe acute respiratory syndrome coronavirus by replication-specific multiplex reverse transcription-PCR. J Clin Microbiol. 2004;42(7):3196-206.
83. De Clercq E, Stewart WE, 2nd, De Somer P. Studies on the mechanism of the priming effect of interferon on interferon production by cell cultures exposed to poly(rI)-poly(rC). Infect Immun. 1973;8(3):309-16.
84. Emeny JM, Morgan MJ. Regulation of the interferon system: evidence that Vero cells have a genetic defect in interferon production. J Gen Virol. 1979;43(1):247-52.
85. Zhu N, Zhang D, Wang W, Li X, Yang B, Song J, et al. A Novel Coronavirus from Patients with Pneumonia in China, 2019. N Engl J Med. 2020;382(8):727-33.
86. Rothan H, Stone S, Natekar J, Kumari P, Arora K, Kumar M. The FDA-approved gold drug Auranofin inhibits novel coronavirus (SARS-COV-2) replication and attenuates inflammation in human cells. bioRxiv. 2020.
87. Tan YJ, Fielding BC, Goh PY, Shen S, Tan TH, Lim SG, et al. Overexpression of 7a, a protein specifically encoded by the severe acute respiratory syndrome coronavirus, induces apoptosis via a caspase-dependent pathway. J Virol. 2004;78(24):14043-7.
88. Yuan X, Wu J, Shan Y, Yao Z, Dong B, Chen B, et al. SARS coronavirus 7a protein blocks cell cycle progression at G0/G1 phase via the cyclin D3/pRb pathway. Virology. 2006;346(1):74-85.
89. Schaecher SR, Mackenzie JM, Pekosz A. The ORF7b protein of severe acute respiratory syndrome coronavirus (SARS-CoV) is expressed in virus-infected cells and incorporated into SARS-CoV particles. J Virol. 2007;81(2):718-31.
90. Pfefferle S, Schopf J, Kogl M, Friedel CC, Muller MA, Carbajo-Lozoya J, et al. The SARS-coronavirus-host interactome: identification of cyclophilins as target for pan-coronavirus inhibitors. PLoS Pathog. 2011;7(10):e1002331.
91. Sung SC, Chao CY, Jeng KS, Yang JY, Lai MM. The 8ab protein of SARS-CoV is a luminal ER membrane-associated protein and induces the activation of ATF6. Virology. 2009;387(2):402-13.
92. Shi CS, Nabar NR, Huang NN, Kehrl JH. SARS-Coronavirus Open Reading Frame-8b triggers intracellular stress pathways and activates NLRP3 inflammasomes. Cell Death Discov. 2019;5:101.
93. Chinese SMEC. Molecular evolution of the SARS coronavirus during the course of the SARS epidemic in China. Science. 2004;303(5664):1666-9.
94. Guan Y, Zheng BJ, He YQ, Liu XL, Zhuang ZX, Cheung CL, et al. Isolation and characterization of viruses related to the SARS coronavirus from animals in southern China. Science. 2003;302(5643):276-8.

95. Lau SK, Feng Y, Chen H, Luk HK, Yang WH, Li KS, et al. Severe Acute Respiratory Syndrome (SARS) Coronavirus ORF8 Protein Is Acquired from SARS-Related Coronavirus from Greater Horseshoe Bats through Recombination. J Virol. 2015;89(20):10532-47.
96. Muth D, Corman VM, Roth H, Binger T, Dijkman R, Gottula LT, et al. Attenuation of replication by a 29 nucleotide deletion in SARS-coronavirus acquired during the early stages of human-to-human transmission. Sci Rep. 2018;8(1):15177.
97. Fu Y, Cheng Y, Wu Y. Understanding SARS-CoV-2-Mediated Inflammatory Responses: From Mechanisms to Potential Therapeutic Tools. Virol Sin. 2020.
98. Chan JF, Kok KH, Zhu Z, Chu H, To KK, Yuan S, et al. Genomic characterization of the 2019 novel human-pathogenic coronavirus isolated from a patient with atypical pneumonia after visiting Wuhan. Emerg Microbes Infect. 2020;9(1):221-36.
99. Falzarano D, de Wit E, Martellaro C, Callison J, Munster VJ, Feldmann H. Inhibition of novel beta coronavirus replication by a combination of interferon-alpha2b and ribavirin. Sci Rep. 2013;3:1686.
100. Gordon CJ, Tchesnokov EP, Feng JY, Porter DP, Gotte M. The antiviral compound remdesivir potently inhibits RNA-dependent RNA polymerase from Middle East respiratory syndrome coronavirus. J Biol Chem. 2020.
101. Yin W, Mao C, Luan X, Shen D-D, Shen Q, Su H, et al. Structural Basis for the Inhibition of the RNA-Dependent RNA Polymerase from SARS-CoV-2 by Remdesivir. bioRxiv. 2020.
102. Shannon A, Tuyet Le NT, Selisko B, Eydoux C, Alvarez K, Guillemot JC, et al. Remdesivir and SARS-CoV-2: structural requirements at both nsp12 RdRp and nsp14 Exonuclease active-sites. Antiviral Res. 2020:104793.
103. Holshue ML, DeBolt C, Lindquist S, Lofy KH, Wiesman J, Bruce H, et al. First Case of 2019 Novel Coronavirus in the United States. N Engl J Med. 2020;382(10):929-36.
104. Kim AHJ, Sparks JA, Liew JW, Putman MS, Berenbaum F, Duarte-Garcia A, et al. A Rush to Judgment? Rapid Reporting and Dissemination of Results and Its Consequences Regarding the Use of Hydroxychloroquine for COVID-19. Ann Intern Med. 2020.
105. Yao X, Ye F, Zhang M, Cui C, Huang B, Niu P, et al. In Vitro Antiviral Activity and Projection of Optimized Dosing Design of Hydroxychloroquine for the Treatment of Severe Acute Respiratory Syndrome Coronavirus 2 (SARS-CoV-2). Clin Infect Dis. 2020.
106. Wellems TE, Plowe CV. Chloroquine-resistant malaria. J Infect Dis. 2001;184(6):770-6.
107. Al-Bari MA. Chloroquine analogues in drug discovery: new directions of uses, mechanisms of actions and toxic manifestations from malaria to multifarious diseases. J Antimicrob Chemother. 2015;70(6):1608-21.
108. de Wilde AH, Pham U, Posthuma CC, Snijder EJ. Cyclophilins and cyclophilin inhibitors in nidovirus replication. Virology. 2018;522:46-55.
109. van Hemert MJ, van den Worm SH, Knoops K, Mommaas AM, Gorbalenya AE, Snijder EJ. SARS-coronavirus replication/transcription complexes are membrane-protected and need a host factor for activity in vitro. PLoS Pathog. 2008;4(5):e1000054.

Figure legends

Fig. 1. Rapid evolution of SARS-CoV-2 during passaging in Vero E6 cells. (a) Outline of a plaque picking experiment that was initiated when the p2 stock of SARS-CoV-2 Australia/VIC01/2020 showed remarkable plaque heterogeneity on Vero E6 cells (leftmost well). Following a plaque assay of the p1 virus stock, small and large plaques were picked and these virus clones were passaged three times in Vero E6 cells, while their plaque phenotype was monitored. In contrast to the large plaque viruses (example L8; bottom row), the plaque phenotype of the small plaque viruses (example S5; top row) rapidly evolved within these 3 passages. (b) Evolution/adaptation of the S protein gene during Vero E6 passaging. Overview of NGS data obtained for the p2 stock, S5p1/p2/p3 and S8p1 in the S1/S2 region of the SARS-CoV-2 S protein gene that encodes the so-called 'furin-like cleavage site. The analysis was based on NGS reads spanning nt 23,576 to 23,665 of the SARS-CoV genome (see Methods for details) and their translation in the S protein open reading frame. Deletions are indicated with Δ followed by the affected amino acid residues.

Fig. 2. Comparison of SARS-CoV-2 and SARS-CoV replication kinetics in Vero E6 cells. (a) Growth curve showing the release of infectious viral progeny into the medium of infected Vero E6 cells (m.o.i. 3), as determined by plaque assay (n = 4; mean ± sd is presented). (b) . Comparison of SARS-CoV-2 Australia/VIC01/2020 and SARS-CoV Frankfurt-1 plaque phenotype in Vero E6 cells.

Fig. 3. Kinetics of SARS-CoV-2 and SARS-CoV RNA synthesis in infected Vero E6 cells. (a) Hybridization analysis of viral mRNAs isolated from SARS-CoV-2- and SARS-CoV-infected Vero E6 cells, separated in an agarose gel and probed with a radiolabelled oligonucleotide recognizing the genome and subgenomic mRNAs of both viruses. Subsequently, the gel was re-hybridized to a probe specific for 18S ribosomal RNA, which was used as a loading control.

964 (b) Analysis of the relative abundance of each of the SARS-CoV-2 and SARS-CoV transcripts.
965 Phosphorimager quantification was performed for the bands of the samples isolated at 12, 14
966 and 24 h p.i., which yielded essentially identical relative abundances. The table shows the
967 average of these three measurements. SARS-CoV-2 mRNA sizes were calculated on the
968 basis of the position of the leader and body transcription-regulatory sequences (ACGAAC) in
969 the viral genome (Sawicki and Sawicki 1995, Xu, Hu et al. 2003).
970
971 **Fig. 4. Cross-reactivity of antisera raised against SARS-CoV structural and non-**
972 **structural proteins.**
973 Selected antisera previously raised against SARS-CoV nsps and structural proteins cross-
974 react with corresponding SARS-CoV-2 proteins. SARS-CoV-2-infected Vero E6 cells (m.o.i.
975 of 0.3) were fixed at 12 or 24 h p.i. For immunofluorescence microscopy, cells were
976 (double)labelled with (a) a rabbit antiserum recognising nsp4 and a mouse mAb recognising
977 dsRNA; (b) anti-nsp4 rabbit serum and a mouse mAb directed against the N protein; (c-e)
978 rabbit antisera recognising against nsp3, nsp13 and the M protein, respectively. Nuclear DNA
979 was stained with Hoechst 33258. Bar, 20 μm.
980
981 **Fig. 5. Visualisation of SARS-CoV-2 and SARS-CoV infection by electron microscopy.**
982 Electron micrographs of Vero E6 cells infected with either SARS-CoV-2 or SARS-CoV at the
983 indicated time points (c-r). Images from a mock-infected cell are included for comparison (a-
984 b). (c-j) RRegions containing viral replication organelles. These virus-induced structures
985 accumulated in large clusters in the perinuclear region by 8 h p.i. (c, g, boxed regions enlarged
986 in d and h, respectively). These regions primarily contained DMVs (d-e, h-i, black asterisks).
987 Additionally, virus-induced convoluted membranes (e, white arrowhead) were observed in
988 SARS-CoV infection, whereas zippered ER (i, white arrowheads) appeared to be more
989 common in SARS-CoV-2-infected cells. At 10 h p.i., vesicle packets (f, j, white asterisks),
990 which seem to arise by fusion of two or more DMVs through their outer membrane, became
991 abundant in the RO regions. (k-r) Examples of virion assembly and release in infected cells.

Virus particles budding into membranes of the ERGIC (k-l, o-p, arrowheads). The black arrowheads in the boxed areas highlight captured budding events, enlarged in l and p. Subsequently, virus particles are transported to the plasma membrane which, at 10 h p.i., is surrounded by a large number of released virions (m, q, boxed areas enlarged in n and r, respectively). N, nucleus; m, mitochondria; G, Golgi apparatus. Scale bars: 1 µm (a, c, g); 500 nm (b, d-f, h-j, k, m, o, q); 100 nm (l, n, p, r).

Fig. 6. Assay to screen for compounds that inhibit SARS-CoV-2 replication.

Inhibition of SARS-CoV-2 replication (coloured bars) was tested in Vero E6 cells by developing a CPE-reduction assay and evaluating several previously identified inhibitors of SARS-CoV, which was included for comparison (grey bars). For each compound a two-fold serial dilution series in the low-micromolar range was tested; (a) Remdesivir, (b) chloroquine, (c) Alisporivir and (d) pegylated interferon alpha-2. Cell viability was assayed using the CellTiter 96® Aqueous One Solution cell proliferation assay (MTS assay). Compound toxicity (solid line) was evaluated in parallel using mock-infected, compound-treated cells. The graphs show the results of 3 independent experiments, each performed using quadruplicate samples (mean ± SD are shown).

1009 **Table 1.** SARS-CoV-specific antisera used and their cross-reactivity with corresponding

1010 SARS-CoV-2 targets.

SARS-CoV antiserum	function of target	antigen type	antibody type	IFA signal*	reference
nsp3 (DGD7)	transmembrane replicase protein, containing PL^{pro}	bacterial expression product	rabbit polyclonal	++	(47)
nsp4 (FGQ4)	transmembrane replicase protein	synthetic peptide	rabbit polyclonal	++	(109)
nsp5 (DUE5)	M^{pro}	bacterial expression product	rabbit polyclonal	+	(47)
nsp6 (GBZ7)	transmembrane replicase protein	synthetic peptide	rabbit polyclonal	-	(109)
nsp8 (DUK4)	RNA polymerase co-factor	bacterial expression product	rabbit polyclonal	++	(47)
nsp8 (39-12)	RNA polymerase co-factor	bacterial expression product	mouse monoclonal	++	unpublished
nsp9 (HLJ5)	RNA-binding protein	synthetic peptide	rabbit polyclonal	++	unpublished
nsp13 (CQS2)	RNA helicase	synthetic peptide	rabbit polyclonal	++	(47)
nsp15 (HLT5)	endoribonuclease	bacterial expression product	rabbit polyclonal	+	unpublished
nsp15 (BGU6)	endoribonuclease	synthetic peptide	rabbit polyclonal	+	(47)
M (EKU9)	membrane protein	synthetic peptide	rabbit polyclonal	+	(47)
N (JUC3)	nucleocapsid protein	bacterial expression product	rabbit polyclonal	+	(35)
N (46-4)	nucleocapsid protein	bacterial expression product	mouse monoclonal	++	(41)

1011 * ++, strongly positive; +, positive; -, negative.

a

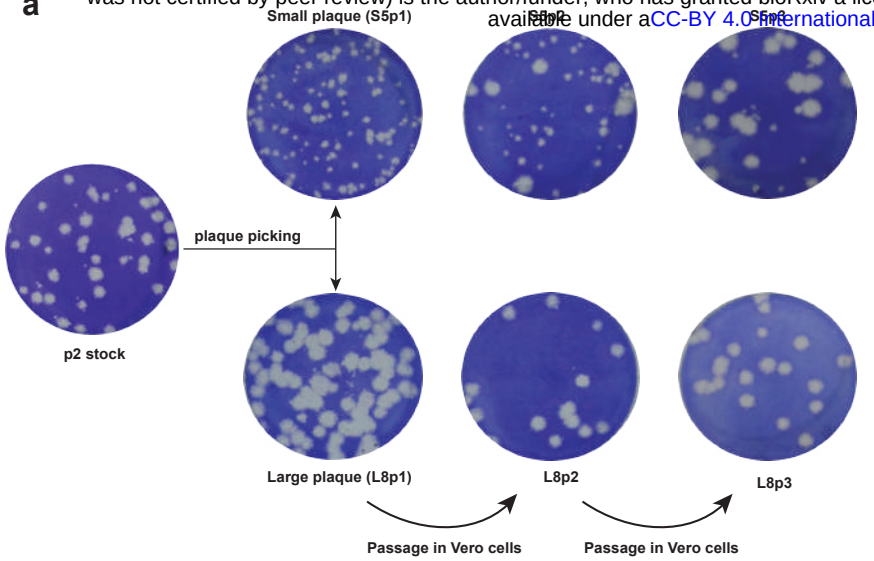

b

672-ASYQTQTNSPRRAR↓SVASQSIIAYTMSLGA-702					
Mutation in furin-like cleavage site region	p2 stock	S5p1	S5p2	S5p3	L8p1
Wild type	44.4%	100%	93.9%	56.5%	13.2%
R682Q	48.3%		2.1%	11.6%	86.8%
R682W	3.8%		1.5%	4.3%	
R682P				1.7%	
R683L			0.9%	1.5%	
R685L	1.4%				
R685P	0.6%				
675-679ΔQTQTN	1.5%		0.8%	2.2%	
679-688ΔNSPRRARSVA			0.7%	22.3%	

Figure 1

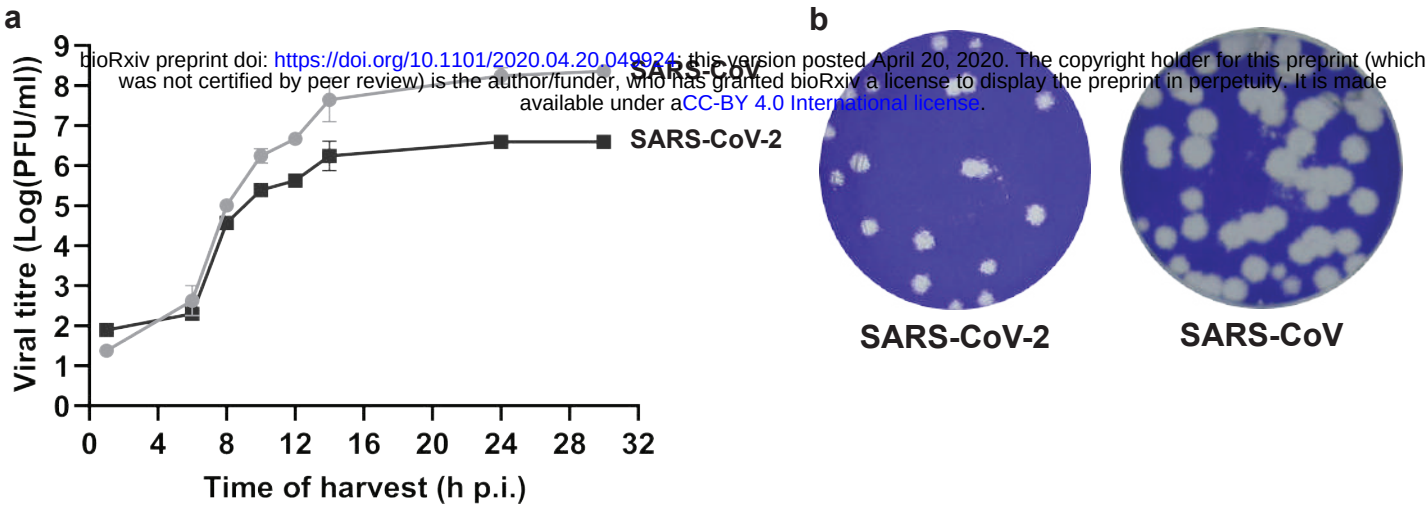

Figure 2

a

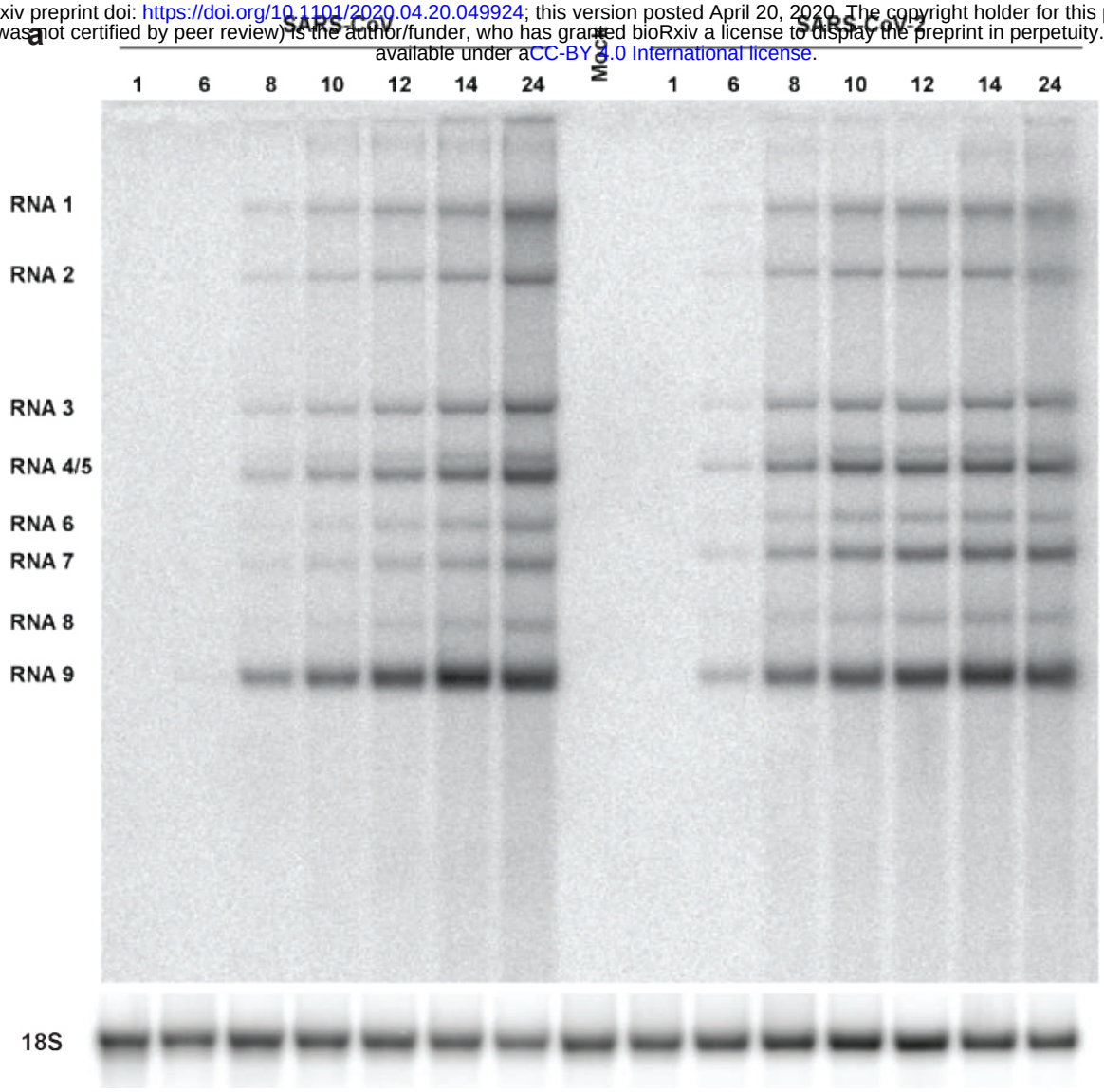

b

RNA	Size (kb) of SARS-CoV-2 mRNA	Relative abundance (%)	
		SARS-CoV	SARS-CoV-2
1	29.9	6.0	5.1
2	8.4	4.0	3.5
3	4.5	7.2	6.9
4	3.7	1.9	2.0
5	3.4	14.2	18.0
6	2.9	2.0	2.5
7	2.5	3.5	13.7
8	2.0	1.1	2.3
9	1.7	60.0	45.9

Figure 3

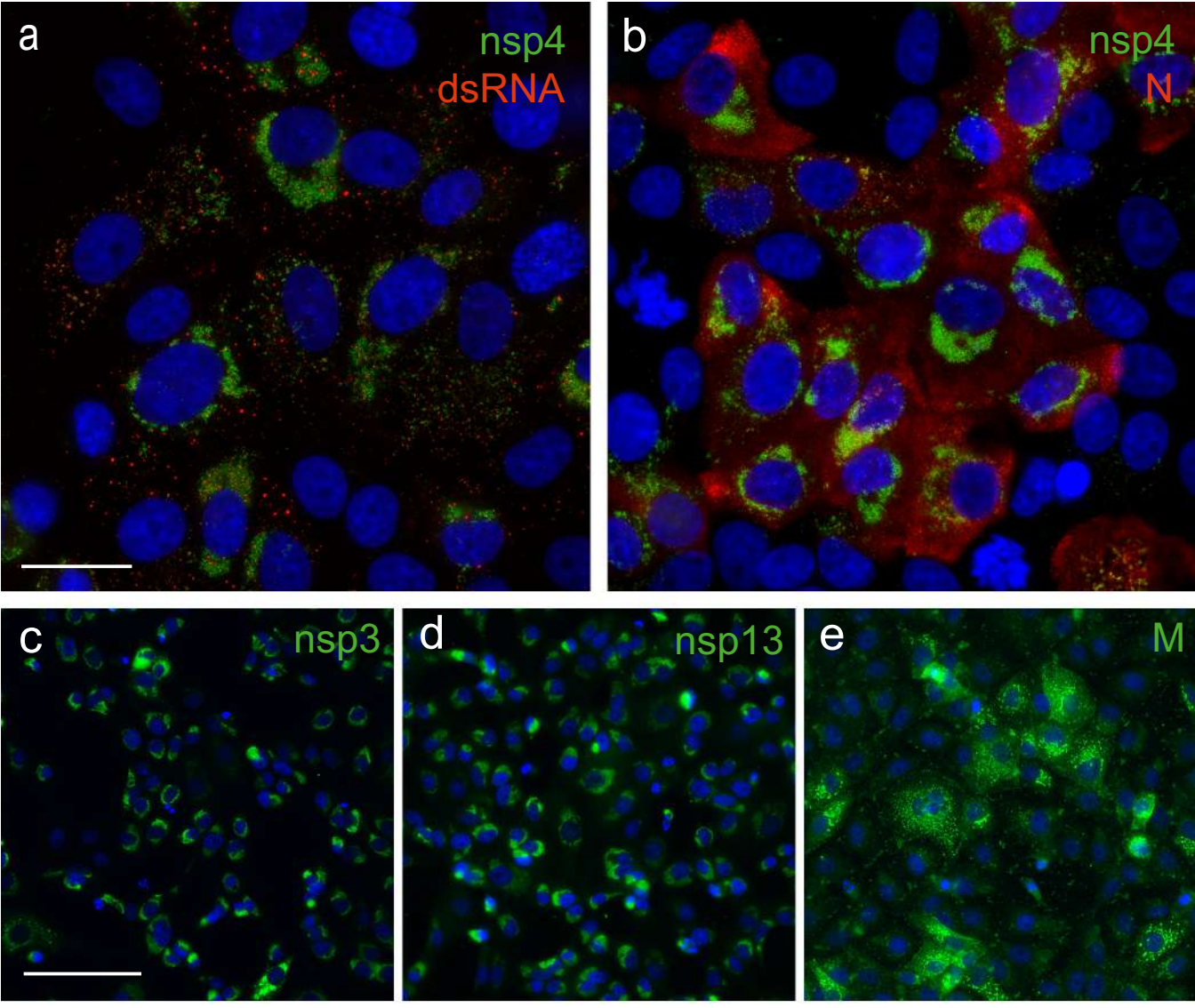

Figure 4

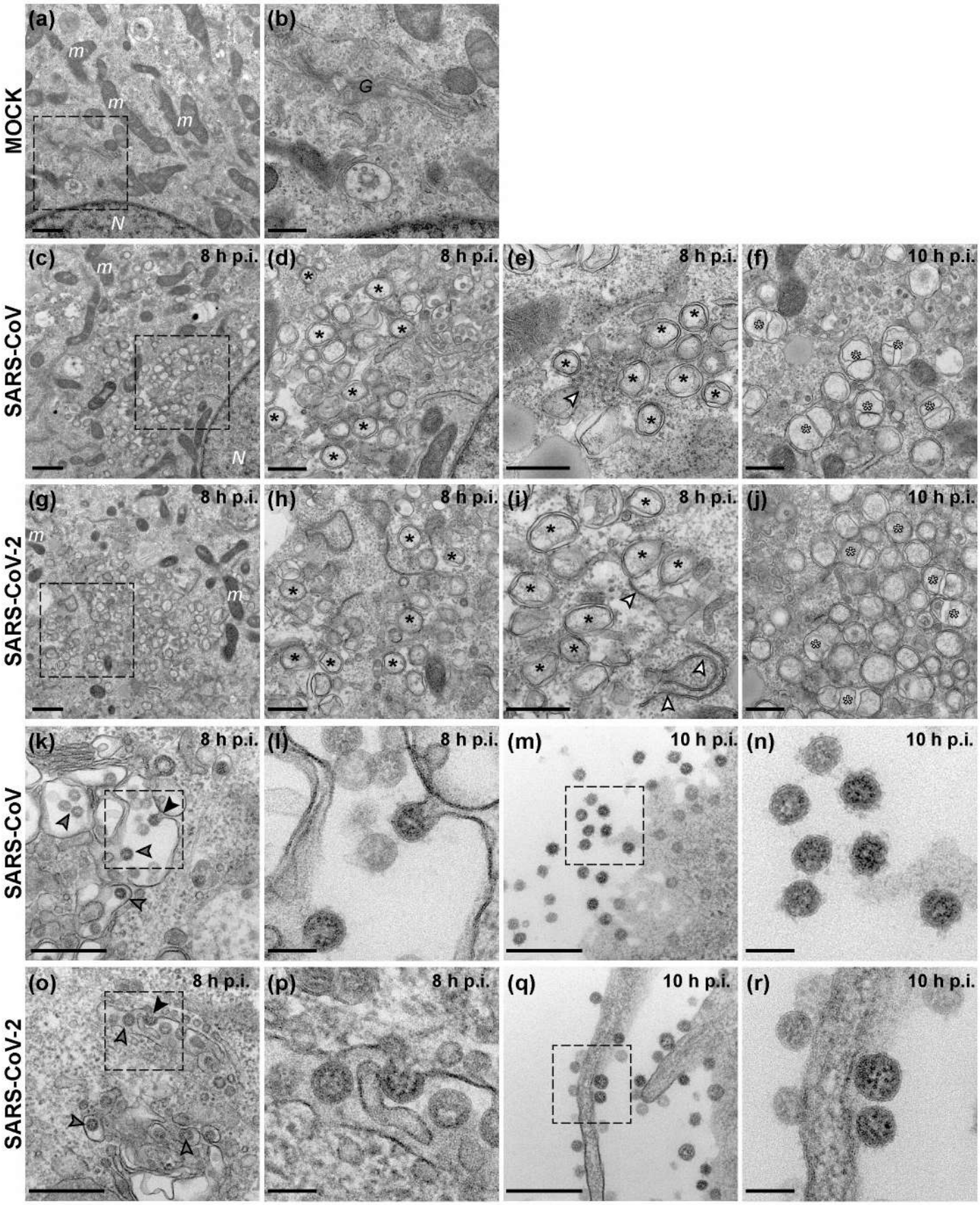

Figure 5

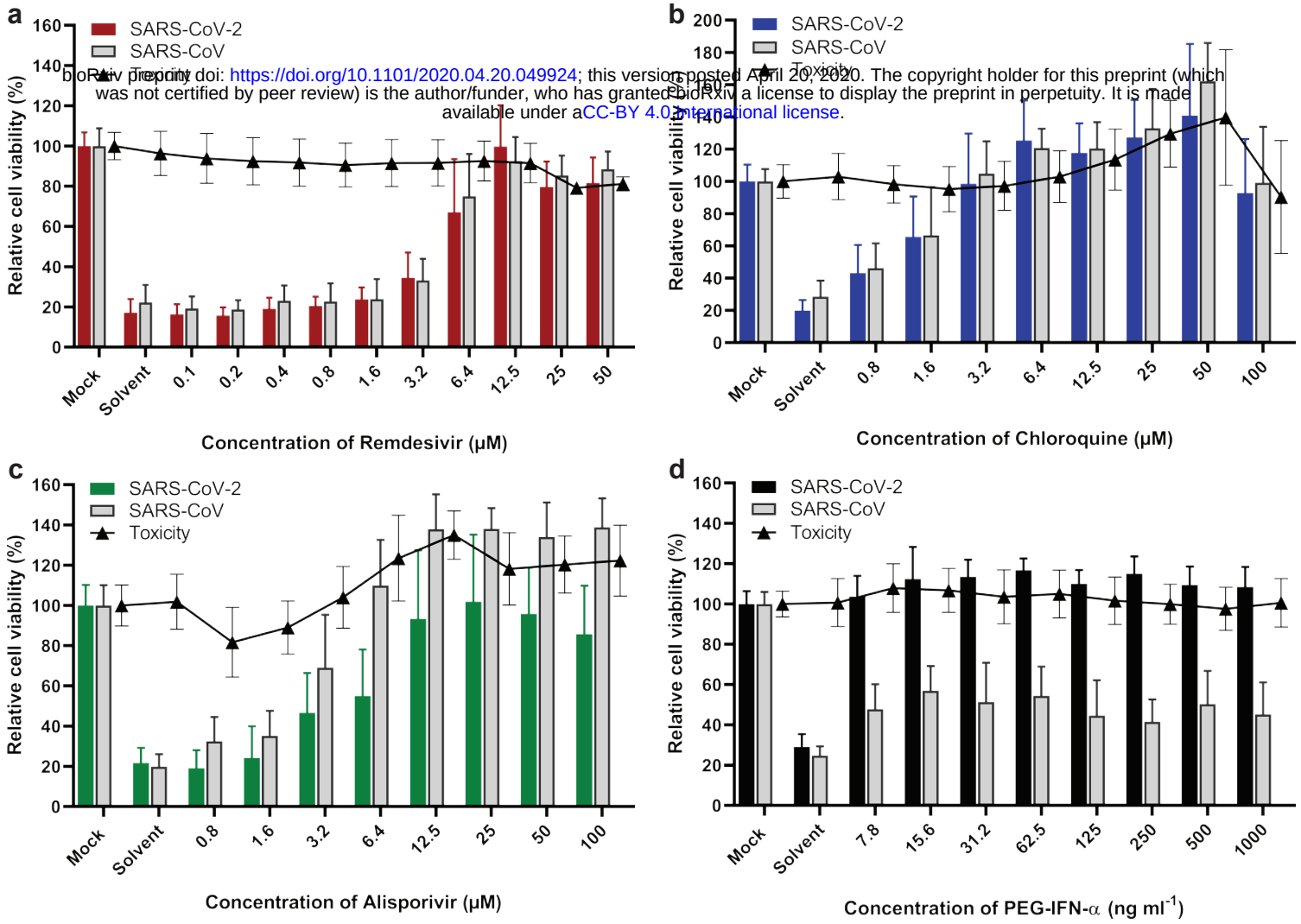

Figure 6